

## Toward BaSi<sub>2</sub>/Si Heterojunction Thin-Film Solar Cells

### Insights into Heterointerface Investigation, Barium Depletion, and Silicide-Mediated Silicon Crystallization

Tian, Yilei; Bento Montes, Ana Rita; Vančo, Ľubomír; Čaplovičová, Mária; Vogrinčič, Peter; Šutta, Pavol; Satrapinskyy, Leonid; Zeman, Miro; Isabella, Olindo

#### DOI

[10.1002/admi.202000887](https://doi.org/10.1002/admi.202000887)

#### Publication date

2020

#### Document Version

Final published version

#### Published in

Advanced Materials Interfaces

#### Citation (APA)

Tian, Y., Bento Montes, A. R., Vančo, Ľ., Čaplovičová, M., Vogrinčič, P., Šutta, P., Satrapinskyy, L., Zeman, M., & Isabella, O. (2020). Toward BaSi<sub>2</sub>/Si Heterojunction Thin-Film Solar Cells: Insights into Heterointerface Investigation, Barium Depletion, and Silicide-Mediated Silicon Crystallization. *Advanced Materials Interfaces*, 7(19), 1-11. Article 2000887. <https://doi.org/10.1002/admi.202000887>

#### Important note

To cite this publication, please use the final published version (if applicable).  
Please check the document version above.

#### Copyright

Other than for strictly personal use, it is not permitted to download, forward or distribute the text or part of it, without the consent of the author(s) and/or copyright holder(s), unless the work is under an open content license such as Creative Commons.

#### Takedown policy

Please contact us and provide details if you believe this document breaches copyrights.  
We will remove access to the work immediately and investigate your claim.

# Toward BaSi<sub>2</sub>/Si Heterojunction Thin-Film Solar Cells: Insights into Heterointerface Investigation, Barium Depletion, and Silicide-Mediated Silicon Crystallization

Yilei Tian,\* Ana Rita Bento Montes, Ľubomír Vančo, Mária Čaplovičová, Peter Vogrinčič, Pavol Šutta, Leonid Satrapinsky, Miro Zeman, and Olindo Isabella\*

The knowledge of the structural and compositional details of Si/BaSi<sub>2</sub>/Si heterostructure annealed at high temperature is a prerequisite for BaSi<sub>2</sub> application in heterojunction thin-film solar cells. For this purpose, Si/BaSi<sub>2</sub>/Si heterostructures deposited by magnetron sputtering with different Si layer thickness are submitted to systematic structural and compositional characterizations. Results reveal a BaSi<sub>2</sub>/Si heterointerfacial variation caused by surface oxidation and Ba diffusion at the high temperature. Its effects on the optical and electrical properties of Si/BaSi<sub>2</sub>/Si heterostructure are presented. The outcomes of this work can be extended to BaSi<sub>2</sub> deposited by other techniques, and generate substantial advantages in BaSi<sub>2</sub> development ranging from improvement on material qualities and eventual deployment in thin-film solar cells.

## 1. Introduction

The need to concurrently address effective light absorption, charge generation and transportation, along with the requirement

for a conveniently synthesized material with minimal toxicity and adequate availability, has triggered a research focus toward barium silicide (BaSi<sub>2</sub>). This is regarded as a low-cost alternative to conventional absorber materials.<sup>[1,2]</sup> The semiconducting BaSi<sub>2</sub> is stable in the ambient condition,<sup>[3]</sup> and exhibits an orthorhombic crystal structure. The Si atom is covalently bound with three neighboring Si atoms forming the characteristic tetrahedron [Si<sub>4</sub>]<sup>4-</sup>, then with Ba<sup>2+</sup>.<sup>[4,5]</sup> Besides the essentially elemental abundance, BaSi<sub>2</sub> possesses a bandgap  $E_g \approx 1.3$  eV with a light absorption coefficient ( $\alpha$ ) over  $10^5$  cm<sup>-1</sup> at the visible light region.<sup>[6,7]</sup> Its potential also stems from

excellent charge transport properties, i.e., a long minority carrier lifetime  $\tau$  ( $\approx 10$ – $27$   $\mu$ s), and the corresponding long diffusion length  $L$  ( $\approx 10$   $\mu$ m).<sup>[8–10]</sup> Despite the great potential of BaSi<sub>2</sub>, there is still a huge gap between the fabrication of materials and the realization of efficient solar cells.

Preliminarily computational researches have established various BaSi<sub>2</sub> homojunction and heterojunction solar cell architectures. Despite its intrinsically moderate n-type nature (electron concentration  $n = 10^{15}$ – $10^{17}$  cm<sup>-3</sup>), the conductivity of BaSi<sub>2</sub> can be modified by external doping. Dopants, such as P, Sb, Ga, Cu, and As, can enhance the electron concentration to the range of  $10^{19}$ – $10^{20}$  cm<sup>-3</sup>, while B, Al, Ag, In, etc., would alter it to a p-type conductivity.<sup>[11–18]</sup> Such bipolar conductivity of BaSi<sub>2</sub> facilitates homojunction architectures. Theoretically, the conversion efficiency ( $\eta$ ) of an n-p BaSi<sub>2</sub> homojunction solar cell can reach 22.5–25%.<sup>[1,19]</sup> However, controllable BaSi<sub>2</sub> doping processes were currently carried out only by molecular beam epitaxy (MBE) with in situ coevaporation or ex situ ion implantation of dopants.<sup>[14,16]</sup> Regardless of expensive and complex equipment involved in processes as well as a restriction of c-Si substrate for depositions, additional high-temperature annealing was needed after the doping process, which caused issues such as the segregation of dopants.<sup>[14]</sup> In the attempt to obtain BaSi<sub>2</sub> homojunction solar cells, n<sup>+</sup>-BaSi<sub>2</sub> (20 nm)/p-BaSi<sub>2</sub> (500 nm)/p<sup>+</sup>-BaSi<sub>2</sub> (50 nm) diodes experimentally exhibited an extremely low  $\eta$  of  $\approx 0.1\%$  that could be caused by high volume of defects.<sup>[20]</sup>


To this end, heterojunction architectures, which have an inherent advantage of being free from doping, exhibit a great promise for BaSi<sub>2</sub> solar cell development. The low lattice

Y. Tian, A. R. Bento Montes, Prof. M. Zeman, Dr. O. Isabella  
Photovoltaic Materials and Devices Group  
Delft University of Technology  
Delft, 2628 CD, The Netherlands  
E-mail: y.tian@tudelft.nl; o.isabella@tudelft.nl

A. R. Bento Montes  
Instituto Dom Luis  
University of Lisbon  
Lisbon 1749-016, Portugal

Dr. Ľ. Vančo, M. Čaplovičová, P. Vogrinčič  
University Science Park Bratislava Centre  
Slovak University of Technology in Bratislava  
Bratislava 812 43, Slovak Republic

Dr. P. Šutta  
New Technologies Research Centre  
University of West Bohemia  
Plzeň 306 14, The Czech Republic  
Dr. L. Satrapinsky  
Faculty of Mathematics, Physics and Informatics  
Comenius University in Bratislava  
Bratislava 842 48, Slovak Republic

 The ORCID identification number(s) for the author(s) of this article can be found under <https://doi.org/10.1002/admi.202000887>.

© 2020 The Authors. Published by Wiley-VCH GmbH. This is an open access article under the terms of the Creative Commons Attribution License, which permits use, distribution and reproduction in any medium, provided the original work is properly cited.

DOI: 10.1002/admi.202000887

mismatch between  $\text{BaSi}_2$  and Si promotes the development of the  $\text{BaSi}_2/\text{Si}$  heterojunction.<sup>[21]</sup> Indeed, the highest experimentally obtained  $\text{BaSi}_2$ -based solar cell with  $\eta = 10\%$  was based on a p- $\text{BaSi}_2$ /n-Si heterojunction configuration.<sup>[22]</sup> It needs to be addressed that the n-Si wafer instead of p- $\text{BaSi}_2$  functioned as the light absorber in the solar cell, which failed to take the full advantage of  $\text{BaSi}_2$ . To release the vast potential of  $\text{BaSi}_2$ , various heterojunction thin-film solar cell architectures based on well-established Si solar cell technology have been proposed, wherein  $\text{BaSi}_2$  is employed for light absorption.<sup>[23]</sup> Simulations on the device level have revealed the great promise of  $\text{BaSi}_2/\text{Si}$  solar cells, for instance, a  $\text{p}^+-\text{Si}$  (100 nm)/ $\text{BaSi}_2$  (2000 nm) solar cell can achieve a  $\eta = 22.7\%$ , and an n-Si/ $\text{BaSi}_2$ /p-Si architecture possesses a potential efficiency up to 30.4%.<sup>[19,24]</sup> Heterojunction architectures allow state-of-the-art photovoltaic techniques, such as tandem solar cells, bandgap engineering, and light management, to experimentally obtain these attractive efficiencies.<sup>[25]</sup> Meanwhile, industrially applicable techniques for  $\text{BaSi}_2$  absorber layer deposition, for instance, vacuum evaporation and sputtering, can be feasibly adopted in  $\text{BaSi}_2/\text{Si}$  solar cell manufacturing.<sup>[26–29]</sup> However, the high-temperature condition involved either in film growth or postgrowth annealing processes can result in issues such as elemental interdiffusion and thermal-stress mismatch, which would generally degrade the device performance or, even worse, lead to an inoperative solar cell. To reach the goal of efficient  $\text{BaSi}_2/\text{Si}$  heterojunction thin-film solar cells, it is of significant necessity and urgency to uncover the  $\text{BaSi}_2/\text{Si}$  heterointerface behaviors during the high-temperature process and their effects on film properties.

Herein, we present a heterointerfacial investigation of Si/ $\text{BaSi}_2$ /Si architectures prepared by room-temperature sputtering with postannealing treatments. Comprehensive analyses on structural and compositional variations of Si/ $\text{BaSi}_2$ /Si architectures can reveal substantial physical and chemical reactions between Si and  $\text{BaSi}_2$ . The influence of the Si layer thickness on  $\text{BaSi}_2$  properties also serves as a guide for material development. These pieces of knowledge would contribute to the development of  $\text{BaSi}_2/\text{Si}$  heterojunction solar cells.

## 2. Results and Discussion

**Figure 1** shows the X-ray diffraction (XRD) patterns of Si/ $\text{BaSi}_2$ /Si structures with Si layer thickness ( $d_{\text{Si}}$ ) ranging from 0 to 50 nm. For notation simplicity, samples were denoted as  $\text{BaSi}_2/\text{Si}-d_{\text{Si}}$ , e.g.,  $\text{BaSi}_2/\text{Si}-20$  represented a  $\text{BaSi}_2$  layer that was sandwiched by two 20 nm Si layers. XRD signatures of  $\text{BaSi}_2$  can be observed in all samples, confirming the presence of crystalline  $\text{BaSi}_2$  in the Si/ $\text{BaSi}_2$ /Si structures. All samples exhibit similar XRD peak profiles regardless of peak intensity difference. This suggests that the employment of Si layers does not lead to a substantially compositional variation of Si/ $\text{BaSi}_2$ /Si structures. Besides signals from  $\text{BaSi}_2$ , traces of  $\beta\text{-FeSi}_2$  are also captured.<sup>[30]</sup> The origin of Fe can be from contamination in targets or deposition environments.

Despite being annealed in vacuo, samples still experience surface oxidation owing to vacuum contaminations, i.e., residual  $\text{O}_2$  and  $\text{CO}_2$ .<sup>[29,31]</sup> It results in surface heterogeneity of samples, as depicted by optical microscopic images in Figure S1

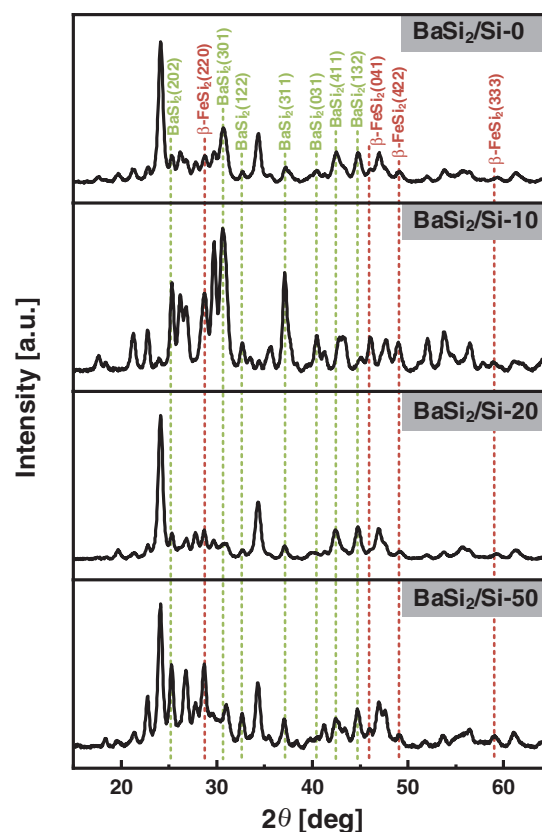


**Figure 1.** XRD patterns of Si/ $\text{BaSi}_2$ /Si samples. Typical peaks from  $\text{BaSi}_2$  and  $\beta\text{-FeSi}_2$  are marked.

(Supporting Information). Raman spectra collected from different positions indicated in Figure S1 (Supporting Information) are presented in **Figure 2**. In a good agreement with XRD results, Raman spectra also reveal the mixed composition of samples. Along with the typical  $\text{BaSi}_2$  Raman peaks, namely,  $F_g$  ( $\approx 276\text{ cm}^{-1}$ ),  $E_g$  ( $\approx 293\text{ cm}^{-1}$ ),  $E_g + F_g$  ( $\approx 355\text{ cm}^{-1}$ ),  $F_g$  ( $\approx 376\text{ cm}^{-1}$ ), and  $A_g$  ( $\approx 486\text{ cm}^{-1}$ ), peaks of  $\beta\text{-FeSi}_2$  at  $247\text{ cm}^{-1}$  and Si nanocrystals (NCs) at  $519\text{ cm}^{-1}$  are observed as well.<sup>[32–34]</sup>

In  $\text{BaSi}_2/\text{Si}-0$ , positions (−3, 7) and (0, 0), which hold different appearances (see Figure S1a, Supporting Information), present the same Raman spectra shape, consisting of strong signals from  $\text{BaSi}_2$ ,  $\beta\text{-FeSi}_2$ , and a weak peak of Si NCs, as shown in Figure 2a. By introducing Si layers,  $\text{BaSi}_2/\text{Si}-10$  and  $\text{BaSi}_2/\text{Si}-20$  present sharper color contrast in microscopic images displayed in Figure S1b,c (Supporting Information), respectively. Such contrast is also reflected by Raman spectra. As shown in Figure 2c,d, position (−5, −2) of  $\text{BaSi}_2/\text{Si}-10$  shows a spectrum without an obvious Si-NCs peak, while the spectrum of position (−2, 2) at  $\text{BaSi}_2/\text{Si}-20$  surface does not contain the peak of  $\beta\text{-FeSi}_2$ . Further increasing  $d_{\text{Si}}$  to 50 nm,  $\text{BaSi}_2/\text{Si}-50$  exhibits a lower color contrast of the surface (see Figure S1d, Supporting Information). And different positions at the surface possess the same Raman spectrum shape, which contains a stronger Si-NCs peak but without the  $\beta\text{-FeSi}_2$  peak compared to that of  $\text{BaSi}_2/\text{Si}-0$ .

Raman microspectroscopic mapping is carried out at the areas indicated in Figure S1 (Supporting Information) to

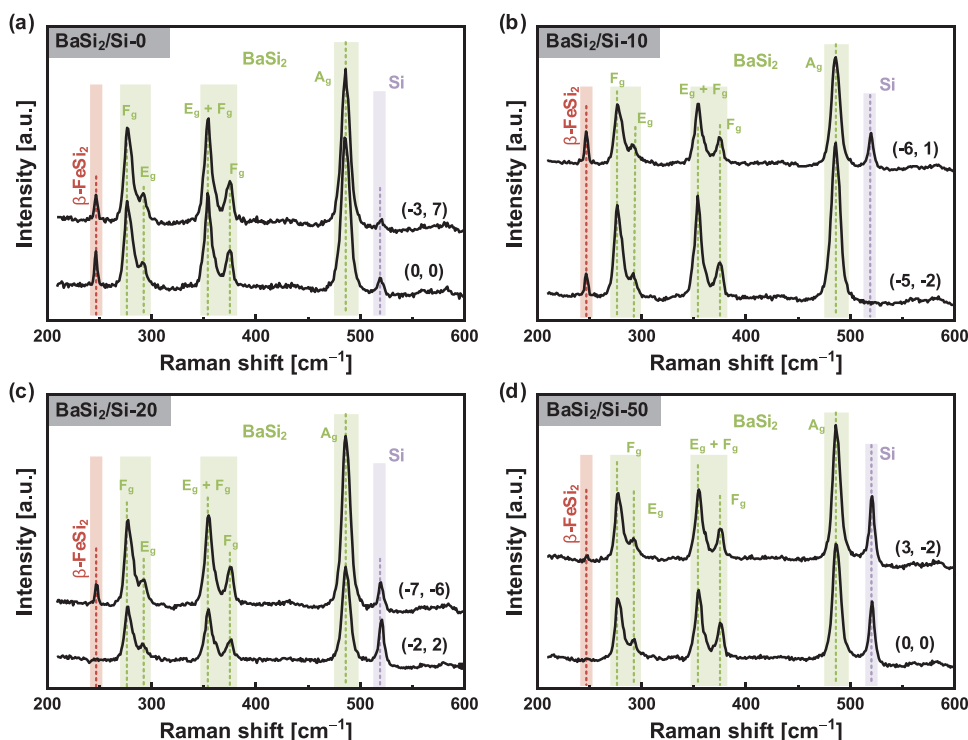


**Figure 2.** a–d) Raman spectra of BaSi<sub>2</sub>/Si-0, BaSi<sub>2</sub>/Si-10, BaSi<sub>2</sub>/Si-20, and BaSi<sub>2</sub>/Si-50. Raman spectra were collected from different areas at the surface of samples.

analyze the surface heterogeneity of samples. Intensities of the characteristic vibrational peaks from BaSi<sub>2</sub> ( $A_g$ ,  $\approx 486\text{ cm}^{-1}$ ),  $\beta$ -FeSi<sub>2</sub> ( $\approx 247\text{ cm}^{-1}$ ), and Si NCs ( $\approx 519\text{ cm}^{-1}$ ) are extracted from the fitted spectra. **Figure 3** visualizes their spatial dependencies in the format of pixel-based images.

As shown in Figure 3, Raman peak intensity maps are consistent, as expected, with the color patterns in optical microscopic images (see Figure S1, Supporting Information). BaSi<sub>2</sub>/Si-0 presents relatively low peak-intensity difference over the measured area, corresponding to the same Raman spectrum shape of different positions in Figure 2a. Conversely, two distinct areas, i.e., a Si-rich grain area and a Ba-rich filling area, are shown in maps of BaSi<sub>2</sub>/Si-10. The Si-rich area displays strong Si NCs signal as illustrated by the lighter area in Figure 3j, while the Ba-rich area is more yellowish or reddish in Figure 3b reflecting the higher content of BaSi<sub>2</sub>. Meanwhile, the peak intensity distributions of BaSi<sub>2</sub> (depicted by Figure 3b) and  $\beta$ -FeSi<sub>2</sub> (presented in Figure 3f) are the reverses of that found for Si NCs (displayed in Figure 3j). Understandably, less Si NCs means more Si atoms would be bounded with Ba and Fe. Such covariation of peak intensity between Si NCs with BaSi<sub>2</sub> and  $\beta$ -FeSi<sub>2</sub> is also observed in BaSi<sub>2</sub>/Si-0 and BaSi<sub>2</sub>/Si-20. On the contrary, in BaSi<sub>2</sub>/Si-50, the area that presents a stronger intensity of Si NCs also exhibits higher intensities of BaSi<sub>2</sub> and  $\beta$ -FeSi<sub>2</sub>. One can assert that the compositional and structural alteration of Si/BaSi<sub>2</sub>/Si structure is closely tied up to the thickness of the Si layer.

The detailed statistical distributions of Raman peak intensity are shown in Figure S2 (Supporting Information). With the increase of  $d_{\text{Si}}$ , we note an obvious increase of Si NCs

average intensity, which is understandable given a thicker deposited Si layer. On the other hand, the  $\beta$ -FeSi<sub>2</sub> intensity drastically declines, which is almost down to zero in BaSi<sub>2</sub>/Si-50. Thus, the thicker Si layer can efficiently suppress the formation of impurity  $\beta$ -FeSi<sub>2</sub> at the surface region. It needs to be addressed that  $d_{\text{Si}}$  does not significantly influence the BaSi<sub>2</sub> peak intensity.

**Figure 4** shows backscattered electron composition mode (BEI-Compo) and secondary electron images (SEI) images of BaSi<sub>2</sub>/Si-0, BaSi<sub>2</sub>/Si-10, and BaSi<sub>2</sub>/Si-50. In the BEI-Compo images, dark areas hold the lower mean atomic number that herein corresponds to the Si-rich composition with a depth of around 100 nm, which is consistent with the Auger depth profiles in **Figure 5**. While, light areas are Si-depleted and therefore present the Ba-rich composition. As presented in Figure 4a, the surface of BaSi<sub>2</sub>/Si-10 consists of Si-rich grain areas and Ba-rich filling areas, which also perfectly coincides with the results of Raman mapping (see Figure 3b,j). With the increase of  $d_{\text{Si}}$ , Ba releases from the prepared structure during annealing, not only in-between the Si-rich grains but also in their centers, as shown in Figure 4b. In Figure 4c related to sample BaSi<sub>2</sub>/Si-50, Ba is distributed over the majority of the surface.

The Ba diffusion also induced an obvious change of surface morphology. Compared to the surface of BaSi<sub>2</sub>/Si-10 (see Figure 4d), Ba-rich islands are distributed in the surface of BaSi<sub>2</sub>/Si-20, illustrated by the light dots in Figure 4e. The size of Ba-rich islands becomes smaller at the surface of BaSi<sub>2</sub>/Si-50 shown in Figure 4f. This also resulted in different surface roughness. BaSi<sub>2</sub>/Si-10, BaSi<sub>2</sub>/Si-20, and BaSi<sub>2</sub>/Si-50 hold  $R_q$  values of 38.27, 1675, and 52.08 nm, respectively. The



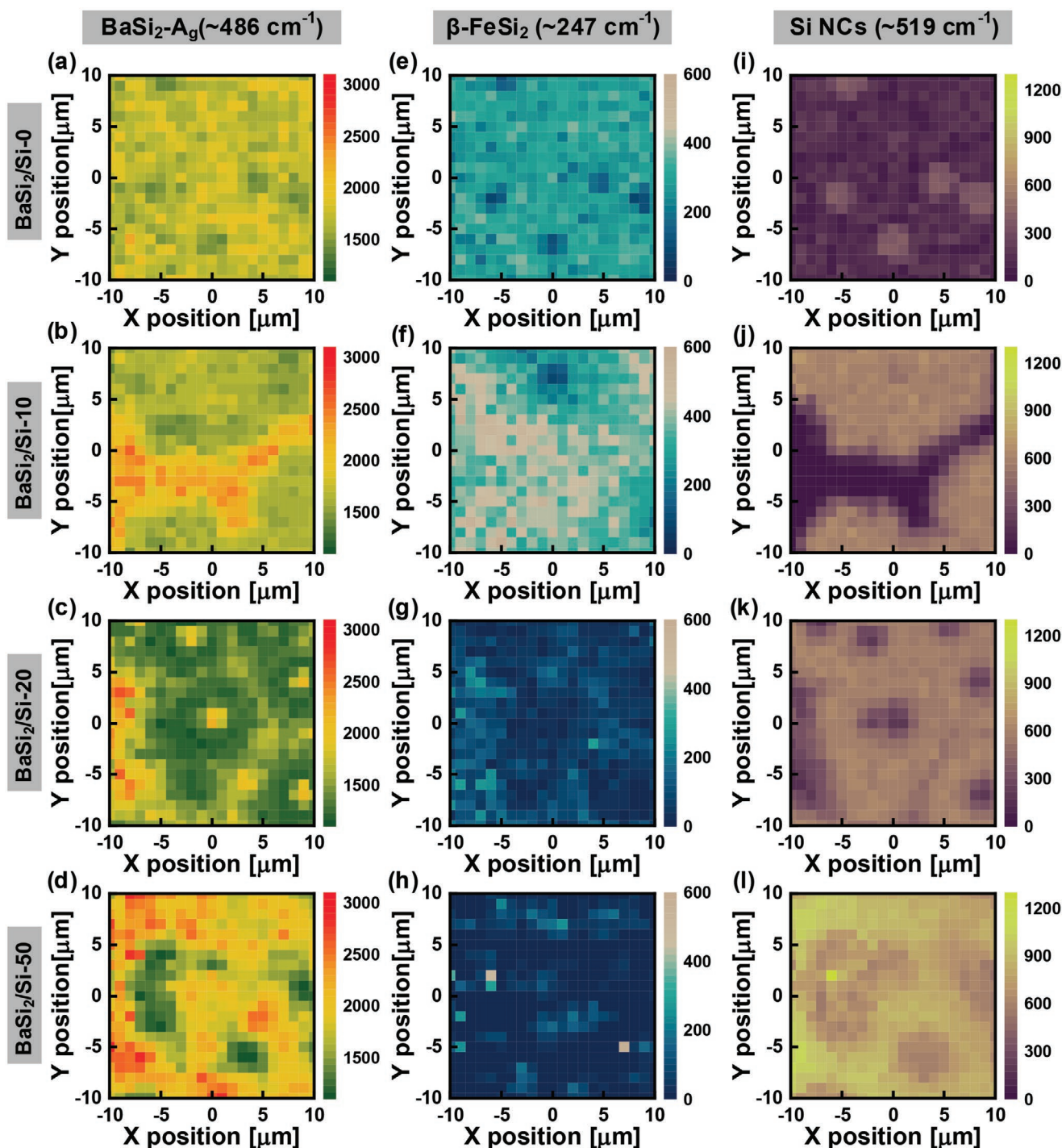


**Figure 3.** Raman mapping of peak intensity distributions of a–d) the strongest vibrational band of  $\text{BaSi}_2$   $A_g$  at  $\approx 486 \text{ cm}^{-1}$ , e–h)  $\beta\text{-FeSi}_2$  band at  $\approx 247 \text{ cm}^{-1}$ , and i–l) Si NCs band at  $\approx 519 \text{ cm}^{-1}$  in a series of deposited a-Si thicknesses of 0, 10, 20, and 50 nm. A measured area of  $20 \times 20 \mu\text{m}^2$  is shown in each case, along with the scale bar labeled with peak intensity in arbitrary unit. The Raman map pixel size is  $1 \times 1 \mu\text{m}^2$ .

wide distribution of small-size Ba-rich islands at  $\text{BaSi}_2/\text{Si-0}$  surface decreases its surface roughness compared to that of  $\text{BaSi}_2/\text{Si-20}$ .

Figure 5a,b depicts the Auger electron spectroscopy (AES) compositional depth profiles of the Ba-rich and Si-rich areas from  $\text{BaSi}_2/\text{Si-10}$  presented in Figure 4a, respectively. A surface

oxide layer, majorly composed of  $\text{BaO}$  and  $\text{SiO}_2$ , can be noticed in both areas. Differently, a Si layer that is buried under the oxide layer, here denoted as sup-Si, can be observed in Figure 5b. The presence of the sup-Si layer leads to the Si-rich composition of that area. Additionally, the Si-rich area presents a thinner surface oxide layer compared to that of the Ba-rich

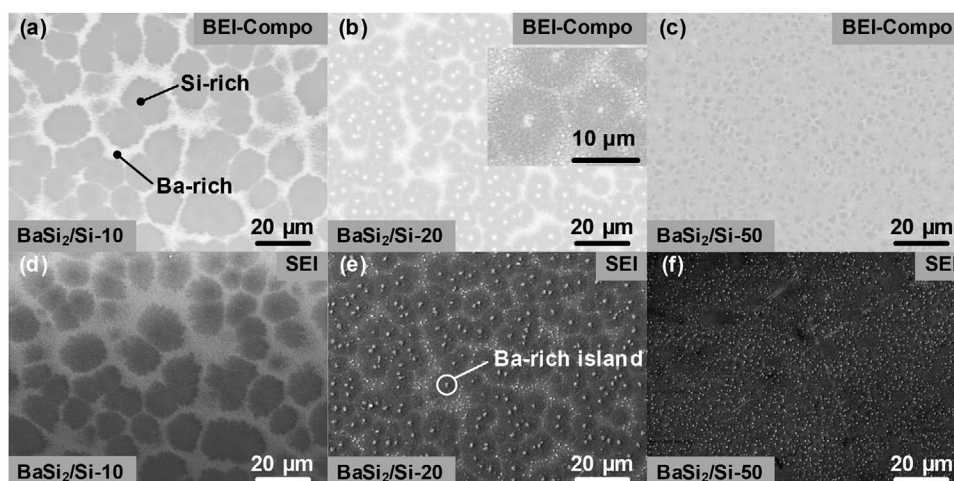


**Figure 4.** Top-view SEM images under imaging conditions of BEI-Compo mode a)  $\text{BaSi}_2/\text{Si-10}$ , b)  $\text{BaSi}_2/\text{Si-20}$ , and SEI mode for c)  $\text{BaSi}_2/\text{Si-10}$ , and for d)  $\text{BaSi}_2/\text{Si-10}$ , e)  $\text{BaSi}_2/\text{Si-20}$ , and f)  $\text{BaSi}_2/\text{Si-50}$ .

area. This is related to the existence of the sup-Si layer that hinders the growth of the oxide layer.

Indeed, the surface oxide layer thickness decreases with the increase of  $d_{\text{Si}}$ , which is reasonable given the thicker sup-Si layer resulting from the growing supply of Si atoms. Eventually,  $\text{BaSi}_2/\text{Si-50}$  exhibits an extremely thin surface oxide layer (less than 10-nm thick), as presented in Figure 5d. Thicker deposited Si layer can effectively alleviate surface oxidation of the Si/ $\text{BaSi}_2$ /Si structure. Owing to the rough surface morphology, it is difficult to carry out AES analysis at different areas of

samples  $\text{BaSi}_2/\text{Si-20}$  and  $\text{BaSi}_2/\text{Si-50}$  shown in Figure 4. The analyzed areas of them are displayed in Figure S3 (Supporting Information).

Looking deeply into the Si(–Si) profile in Figure 5d, one can notice a Si(–Si) concentration dip at the depth of around 50 nm. This dip corresponds to a concentration increase of BaO. Thus, the surface region is consequently divided into a double-Si-layers structure by the BaO layer. Moreover, Ba(–Si), as an indicator of  $\text{BaSi}_2$  existence, can also be detected within the sup-Si layer. The formation of  $\text{BaSi}_2$  and BaO in the sup-Si

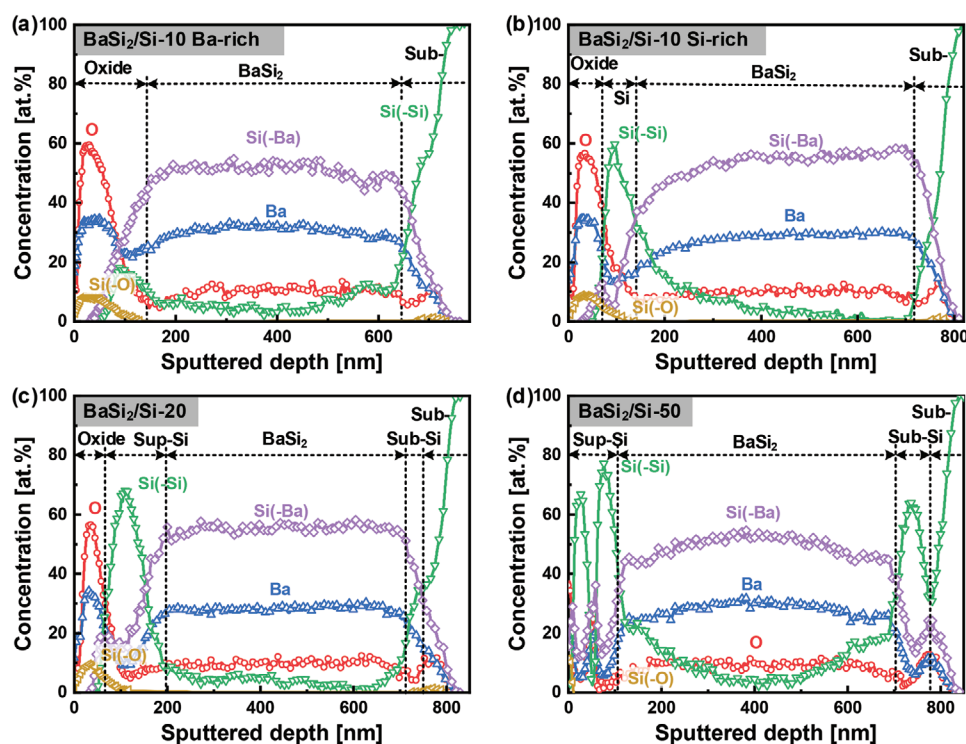


**Figure 5.** Auger electron spectroscopy compositional depth profiles of a)  $\text{BaSi}_2/\text{Si-10}$  Ba-rich area, b)  $\text{BaSi}_2/\text{Si-10}$  Si-rich area, c)  $\text{BaSi}_2/\text{Si-20}$ , and d)  $\text{BaSi}_2/\text{Si-50}$ . Si(–Ba), Si(–Si), and Si(–O) represent Si atoms that are bonded with Ba, Si, and O, respectively.



layer can result from the Ba diffusion, which is in great agreement with the Ba-release phenomenon revealed by scanning electron microscopy (SEM) images presented in Figure 4.

On the other side of the Si/BaSi<sub>2</sub>/Si sandwich structure, Ba atoms also penetrate through the bottom Si layer, denoted as sub-Si, and even diffuse into the polycrystalline Si (poly-Si) substrate. Such phenomena of Ba diffusion into the substrate layer are observed in all samples. Interestingly, the shapes of elemental profiles, including Si(–Ba), Ba, Si(–Si) in the sample BaSi<sub>2</sub>/Si-50, indicate an overall similarity of structural transformation between sup-Si/BaSi<sub>2</sub> and BaSi<sub>2</sub>/sub-Si interfaces. This reasonably stands for the effectiveness of the thicker sup-Si layer for oxygen exclusion in the BaSi<sub>2</sub> surface region.

Apart from heterointerface, BaSi<sub>2</sub> bulk from all samples displays a good stoichiometry of Ba/Si = 1/2. Note that oxygen atoms are incorporated with BaSi<sub>2</sub> in all samples with an atomic concentration of around 10%. According to our previous study, oxygen here is originated from the sputtering process, as it can be detected in as-deposited samples as well (see Figure S4, Supporting Information).<sup>[29,31]</sup>

Elemental distributions of impurities, including Fe, N, and C, are profiled in Figure S5 (Supporting Information). In the as-deposited sample, impurities of only Fe and N are detected.

Fe, in the form of  $\beta$ -FeSi<sub>2</sub>, is uniformly distributed throughout the BaSi<sub>2</sub> bulk with an atomic concentration of  $\approx$ 4%. It suggests that Fe is likely from the BaSi<sub>2</sub> target. While N is only detected in the Si layer. It is hard to speculate its origin from either the Si target or vacuum contaminations. On the other hand, C is mainly noticed in the very surface region of samples, which can be a consequence of the reactions between Ba and CO<sub>2</sub> from the annealing atmosphere plus the very thin surface contamination of hydrocarbons present in whichever sample.

Cross-sectional scanning transmission electron microscopy (STEM) results are shown in Figure 6. The BaSi<sub>2</sub> crystallite in BaSi<sub>2</sub>/Si-20, as shown in Figure 6a, is determined to be orthorhombic (Powder diffraction file, PDF No. 98 009 4260) by the evaluation of the relevant fast Fourier transform (FFT) pattern. The bright-field (BF) STEM image of the BaSi<sub>2</sub> layer shown in Figure 6b, associated with its corresponding energy-dispersive X-ray spectroscopy (EDS) analyses reported in Figure 6c–f, confirms the compositional state consisting of BaSi<sub>2</sub>, BaO,  $\beta$ -FeSi<sub>2</sub>, Si-NCs, as well as amorphous phase of Si (a-Si).

The BaSi<sub>2</sub>/sub-Si/poly-Si interfacial structure of BaSi<sub>2</sub>/Si-20 is shown in Figure 6g. The 20 nm sub-Si layer can be noticed, which majorly presents an amorphous state with limited

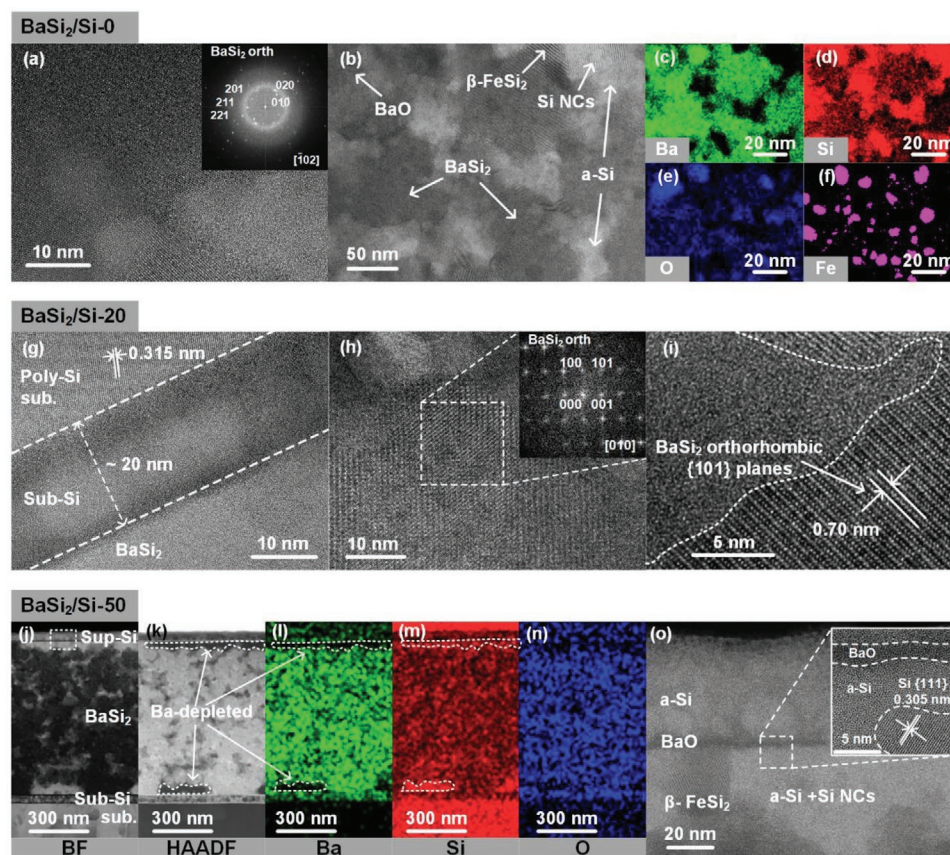


**Figure 6.** a) BF-STEM image of BaSi<sub>2</sub>/Si-0 with the corresponding FFT pattern. b) BF-STEM image of BaSi<sub>2</sub> layer of BaSi<sub>2</sub>/Si-0. c–f) STEM-EDS maps of Ba, Si, O, and Fe, respectively, from the area in (b). g) BF-STEM image of the interfacial region of the poly-Si/Si/BaSi<sub>2</sub> of sample BaSi<sub>2</sub>/Si-20. h) HRTEM image of BaSi<sub>2</sub> layer in BaSi<sub>2</sub>/Si-20. Inset is the FFT obtained from the dashed-line boxed area. i) HRTEM image of crystalline BaSi<sub>2</sub> and the amorphous phase. j) BF-STEM image, k) HAADF-STEM image, and corresponding EDS maps of l–o) Ba, Si, and O, respectively, from sample BaSi<sub>2</sub>/Si-50. o) BF-STEM image of BaSi<sub>2</sub>/Si-50 surface indicated by the boxed area of (j), the inset is the HR-STEM image of the boxed area in (o).

crystalline phases. The brightness contrast of the sub-Si layer suggests the existence of heavier atoms likely Ba owing to its diffusion into the Si layer. Figure 6h is a high-resolution transmission electron microscopy (HRTEM) image of BaSi<sub>2</sub> crystallite. The BaSi<sub>2</sub> crystallite size is about 85 nm. Here, BaSi<sub>2</sub> is orthorhombic as well. Figure 6i further presents a mixture of crystalline BaSi<sub>2</sub> grains and amorphous phases. The {101} planes of orthorhombic BaSi<sub>2</sub> with a space of 0.7 nm are shown.

The overall cross-sectional layer structure of BaSi<sub>2</sub>/Si-50 is depicted in Figure 6j,k. From the top down, sup-Si, BaSi<sub>2</sub>, and sub-Si layers can be identified. BF and high-angle annular dark-field (HAADF) STEM images shown in Figure 6j,k, together with EDS maps presented in Figure 6l–n, confirm the layer structure shown in Figure 5d. The Ba penetration into both sup- and sub-Si layers is revealed by Ba distribution in Figure 6l, owing to which Ba-depleted areas form the interfacial regions within the BaSi<sub>2</sub> layer. In fact, such a Ba-depleted area presents a Si-rich composition, in which area isolated Si atoms are partly crystallized as Si NCs. The detailed surface structure is shown in Figure 6o. The surface region is separated by a BaO layer into two layers, corresponding to the double-Si-layers structure in Figure 5d. Further looking into the surface structure, the upper sup-Si layer contains majorly a-Si, while the lower sup-Si layer rather consists of a-Si and Si-NCs (see the inset in Figure 6o), together with β-FeSi<sub>2</sub> crystallites.

Generally, four mechanisms can be distinguished during the structural and compositional alteration of Si/BaSi<sub>2</sub>/Si structures based on the above analyses:

- i. *Early-stage surface oxidation of deposited-Si layer.* Even though the annealing process is carried out in a high-vacuum condition, the eventual presence of contaminations, for instance, O<sub>2</sub> and CO<sub>2</sub>, cannot be ignored. This facilitates the surface

oxidation of the deposited-Si layer. Such Si-layer oxidation occurs at the early stage of the annealing. The major product of the reaction is SiO<sub>2</sub>.

- ii. *Growth of surface oxide layer driven by the Ba diffusion.* The further growth of the oxide layer at the Si surface is determined by the  $d_{\text{Si}}$ . Considering the high-temperature condition during the annealing, the effects of Ba diffusion does count. The case of a thin Si layer, for instance, BaSi<sub>2</sub>/Si-10, is illustrated in Figure 7a. Ba can easily diffuse through the thin Si layer, given the amorphous state of the deposited Si layer and the high diffusivity of Ba. A reasonable large amount of Ba atoms reaches the oxide layer or even the oxide surface. These Ba atoms lead to an oxide layer thickness increase as well as a compositional alteration from SiO<sub>2</sub> to an eventual mixture of SiO<sub>2</sub> and BaO, as shown in Figure 5. Such process follows the reaction paths<sup>[29]</sup>



Eventually, the surface of BaSi<sub>2</sub>/Si-10, no matter Si-rich or Ba-rich areas, is covered with a several-tens-to-hundreds-nanometers oxide layer that is composed of BaO and SiO<sub>2</sub>, as shown in Figure 5a,b. Once the oxide layer is thick enough to cut off the oxygen supply from the annealing environment, the growth rate of oxide decreases, and the oxide reaches a nearly constant thickness.

If the Si is sufficiently thick that a limited amount of Ba can penetrate through it, then the most of the mass transport takes place beneath the oxide and is most likely associated with the Ba movement within the Si layer. This is the case of BaSi<sub>2</sub>/Si-50,

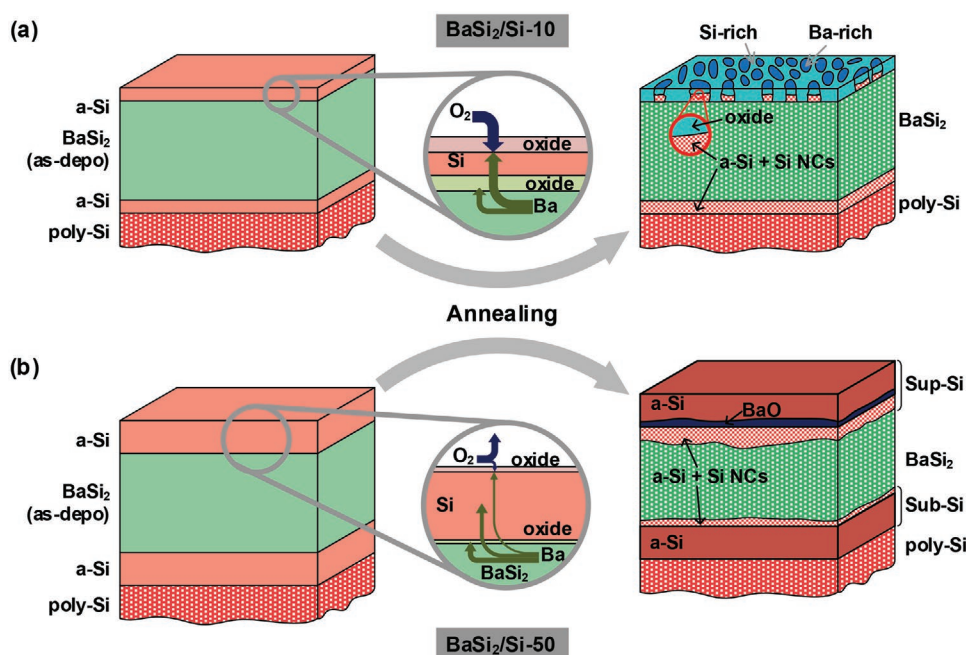


**Figure 7.** Schematic illustration of the structural variation of Si/BaSi<sub>2</sub>/Si heterostructure: a) BaSi<sub>2</sub>/Si-10 and b) BaSi<sub>2</sub>/Si-50 after the thermal annealing process.



visualized in Figure 7b. The oxidation then is confined to the Si surface with a thickness as low as several nanometers as shown in Figure 5d. That limited amount of Ba atoms arrives at the surface and forms the Ba islands shown in Figure 4f.

iii. *Depletion of Ba at oxide/BaSi<sub>2</sub> and Si/BaSi<sub>2</sub> interfaces.* The Ba depletion is caused by the reactions between oxide and Ba that cause the longitudinal diffusion and/or the lateral migration of Ba. Due to the extremely low content of O<sub>2</sub> in the annealing environment ( $p < 10^{-4}$  Pa), we can expect nonuniform surface oxidation of samples. It also leads to a nonuniform oxide growth toward BaSi<sub>2</sub> bulk. As discussed previously, the thin Si layer in BaSi<sub>2</sub>/Si-10 cannot curb the oxide growth into the BaSi<sub>2</sub> bulk. The nonuniformly distributed oxide can drag the Ba to migrate laterally due to the reaction described in Equation (1). Such redistribution of Ba atoms enables the formation of Si-rich areas that are Ba-depleted and the Ba-rich areas that Ba atoms move to. The relatively intensive surface oxidation of BaSi<sub>2</sub>/Si-10 brings a high volume of Ba migration, and then results in obvious Ba-rich and Si-rich areas at its surface as shown in Figure 4a. Conversely, these Ba-rich and Si-rich areas can be hardly distinguished at the surface of BaSi<sub>2</sub>/Si-50, presented in Figure 4c. Although, STEM images imply the existence of Ba-depleted regions at Si/BaSi<sub>2</sub> heterointerfaces in BaSi<sub>2</sub>/Si-50, as shown in Figure 6k,l. The formation of these Ba-depleted regions is related to the native oxide of BaSi<sub>2</sub> and poly-Si substrate. This process is similar to the case of BaSi<sub>2</sub>/Si-10. Differently, the limited amount of oxide restrains the depletion of Ba. And these Ba-depleted regions are buried beneath the thick Si layer or the whole Si/BaSi<sub>2</sub>/Si structure. Thus, there is no obvious Ba-rich or Si-rich area at the BaSi<sub>2</sub>/Si-50 surface. Additionally, reactions at Si/BaSi<sub>2</sub> heterointerface produce the outcome such as BaO, which is indicated by the double-Si-layer structure in Figures 5d and 6o.

iv. *Si isolation and crystallization.* Si atoms are isolated at the BaSi<sub>2</sub> side of the oxide/BaSi<sub>2</sub> and Si/BaSi<sub>2</sub> interface due to the Ba movement. According to AES and STEM analyses, these Si atoms can either stay amorphous state or form Si crystallites owing to the so-called silicide-mediated Si crystallization.<sup>[35,36]</sup> This phenomenon is clearer in BaSi<sub>2</sub>/Si-50. As shown in Figure 6m, an intensive Si signal in the EDS map can be overserved at the Ba-depleted area. And the HRTEM image in Figure 6o further proves the presence of both amorphous and crystalline Si phases. The formation of the amorphous phase is understandable given the original nature of as-deposited BaSi<sub>2</sub>. Before being crystallized, part of Ba diffuses out and leave the amorphous state Si. In the path of propagating to the surface layer, Ba passes by the amorphous state Si and can form BaSi<sub>2</sub> crystallites. Yet, Ba can still diffuse out of BaSi<sub>2</sub> lattice and leads to the formation of Si crystallites, which is similar to the nickel-silicide-mediated Si crystallization.<sup>[35]</sup> To examine it, samples with a structure of 20-nm Si/20-nm BaSi<sub>2</sub>, 20-nm BaSi<sub>2</sub>, and 20-nm Si are annealed at the same condition (600 °C for 30 min). As proven by the Raman spectra in Figure S6 (Supporting Information), only samples endowed BaSi<sub>2</sub> exhibit the peak of Si NCs at  $\approx 519$  cm<sup>-1</sup>. And the strongest Si NCs peak, as expected, is shown in the spectrum of sample Si

(20 nm)/BaSi<sub>2</sub>(20 nm). Isolation and crystallization of Si result in both sup- and sub-Si layers composed of a-Si and Si-NCs in BaSi<sub>2</sub>/Si-50, presented in Figure 7b. Similarly, Si NCs form at Si-rich area at the surface of BaSi<sub>2</sub>/Si-10 illustrated in Figure 7a.

Accordingly, the complex multilayer structures of Si/BaSi<sub>2</sub>/Si samples revealed by previous structural and compositional characterizations are obtained after annealing, which is depicted in Figure 7. Such a multilayer system enables further interface engineering of BaSi<sub>2</sub>, because the BaSi<sub>2</sub> bulk in BaSi<sub>2</sub>/Si-50 is completely protected by the Si layers even at the high-temperature condition.

Figure 8 presents the results of optical and electrical characterizations on annealed Si/BaSi<sub>2</sub>/Si heterostructures. Wavelength-based absorptance curves are displayed in Figure 8a. Reflectance and transmittance curves are shown in Figure S7 (Supporting Information). The thickness of Si does not make a significant difference in the absorptance of samples. A clear absorption edge near the reported bandgap energy of BaSi<sub>2</sub> (1.25 to 1.35 eV) can be observed in the absorptance curve of all samples. The high absorptance around 90% at near-UV and visible spectral windows can be noticed with all Si/BaSi<sub>2</sub>/Si samples, suggesting it as a good light-absorber candidate for photovoltaic applications. Besides interference fringes, absorption tails can also be noticed at the near-infrared (NIR) range, which can result from the remaining metallic and defective phases within the film.

The sputtered Si/BaSi<sub>2</sub>/Si structures still present an n-type semiconducting nature indicated by Hall effect measurements. The n-type conductivity nature of intrinsic BaSi<sub>2</sub> results from Si vacancies that act as donors.<sup>[37]</sup> As shown in Figure 8b, the electron concentration ( $n$ ) varies with Si layer thickness. Since interfacial reactions of Si/BaSi<sub>2</sub>/Si heterostructure are depended on the Si layer thickness, this may alter densities of defect and/or impurities (such as  $\beta$ -FeSi<sub>2</sub>, Si-NCs) in the BaSi<sub>2</sub>, thereby influencing the  $n$ . Meanwhile, the wider  $n$  distribution of BaSi<sub>2</sub>/Si-20 and BaSi<sub>2</sub>/Si-50 can be due to the higher resistivity of the surface layer, consisting of a-Si and BaO, which leads to a higher measurement inaccuracy. The hall mobility ( $\mu_H$ ) of samples is shown in Figure 8c. An enhancement of  $\mu_H$  can be noticed by increasing the  $d_{Si}$ . The thicker Si layer can suppress the surface oxidation and element interdiffusion, which decreases the concentrations of defects and impurities. This results in the enhancement of the Hall mobility.

The temperature dependence of transverse electric conductivity ( $\sigma$ ) at moderate temperatures is measured, as presented in Figure 8d. The lowest conductivity of BaSi<sub>2</sub>/Si-20 can result from the thicker oxidation layer compared to BaSi<sub>2</sub>/Si-50, as well as the thicker multiphase Si layer compared to BaSi<sub>2</sub>/Si-10 and BaSi<sub>2</sub>/Si-0. The highest conductivity of BaSi<sub>2</sub>/Si-10 corresponds to its higher carrier concentration. The conductivity and temperature ( $T$ ) exhibit an Arrhenius behavior

$$\sigma = \sigma_0 \exp(-E_a / kT) \quad (4)$$

where  $k$  is the Boltzmann constant,  $\sigma_0$  is a pre-exponential factor, and  $E_a$  is the characteristic activation energy.  $E_a$  defines

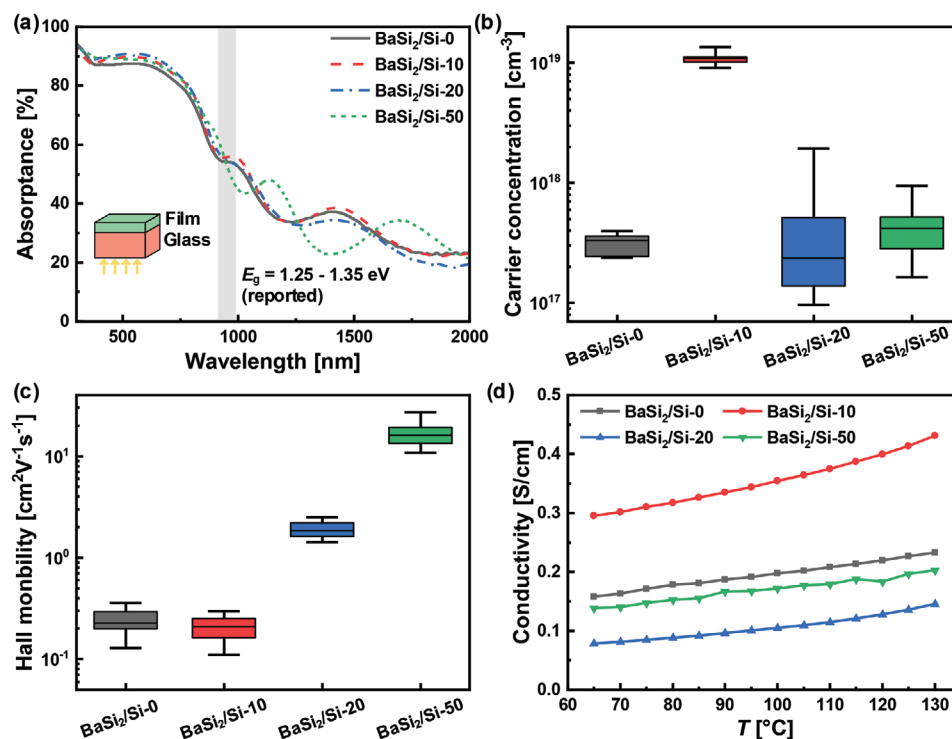


**Figure 8.** Optical and electrical properties of annealed Si/BaSi<sub>2</sub>/Si heterostructures. a) Wavelength-dependent absorbance measured with normal incident radiation from the glass substrate side. The inset sketches the geometry of the optical systems. b,c) Box charts of electron concentration and Hall mobility. The box charts illustrate the interquartile range, median, max, and min values. d) Temperature-dependent electric conductivity at the moderate temperature range.

the activation energy of the grain-boundary-limited conductivity and depends on the donor ionization energy as well as the barrier height between grains. The relation can be rewritten as

$$\ln(1/\sigma) = E_a / kT + \ln(1/\sigma_0) \quad (5)$$

which is also known as the Meyer–Neldel rule.<sup>[38]</sup> Accordingly,  $E_a$  can be derived from  $\ln(1/\sigma)$  versus  $1/kT$  curves (see Figure S8, Supporting Information). All samples present low values of  $E_a$ . BaSi<sub>2</sub>/Si-0, BaSi<sub>2</sub>/Si-10, and BaSi<sub>2</sub>/Si-50 exhibit the  $E_a$  of 68.01, 67.26, and 65.87 meV, respectively. While, BaSi<sub>2</sub>/Si-20 possesses a slightly higher  $E_a$  of 105.77 meV. The difference of  $E_a$  among samples can result from factors such as defect density, grain size, bulk crystallinity, impurities, etc., which need to be further identified.

### 3. Conclusion

Our results offer insights into structural and compositional variations of Si/BaSi<sub>2</sub>/Si architectures which may contribute to the development of thin-film BaSi<sub>2</sub>/Si heterojunction solar cells. Indeed, high-temperature annealing induces drastic structural and compositional variations at BaSi<sub>2</sub>/Si heterointerface wherein film oxidation and Ba depletion alter the elemental distributions and chemical combinations. The thickness of the Si layer influences oxide layer growth, Ba depletion, and multiphase Si layer formation at the heterointerfaces. The out-

comes of this work can be extended to BaSi<sub>2</sub> deposited by other techniques and lead to implementation in photovoltaic applications. This, in turn, may open new opportunities and generate substantial advantages in BaSi<sub>2</sub> development, spinning from improvement on material qualities and deployment in thin-film solar cells.

### 4. Experimental Section

**Fabrications of Si/BaSi<sub>2</sub>/Si Structures:** BaSi<sub>2</sub> and Si layers were deposited by a radio-frequency (RF) magnetron sputtering setup (Kurt J. Lesker) with a stoichiometric BaSi<sub>2</sub> target and an intrinsic Si target, respectively. The sputtering chamber was pumped down to a pressure ( $p$ ) lower than  $5 \times 10^{-4}$  Pa after placing the substrate inside. An Ar gas flow was introduced for sputtering. Prior to the deposition, targets were presputtered for cleaning. The plasma power density and deposition pressure of BaSi<sub>2</sub> and Si were set as  $0.617 \text{ W cm}^{-2}$  and 1 Pa, and  $0.601 \text{ W cm}^{-2}$  and 0.3 Pa, respectively. All films were deposited at room temperature (RT). Depositions of BaSi<sub>2</sub> and Si were carried out in the same chamber without breaking the system vacuum to diminish the impact of surface oxidation. Two Si layers with the same thickness ( $d_{\text{Si}}$ ) ranging from 0 to 50 nm were deposited to sandwich a BaSi<sub>2</sub> layer. Thus, samples with the architecture of Si/BaSi<sub>2</sub>/Si/Substrate were obtained. Subsequent annealing processes were carried out at 600 °C in a high vacuum environment ( $p < 10^{-4}$  Pa) enabling the BaSi<sub>2</sub> crystallization. The thickness of the BaSi<sub>2</sub> layer was kept constant at around 700 nm. That was considered sufficiently thick to isolate surface reactions from bulk crystallization upon high-temperature annealing.

Corning glass and c-Si wafer substrates were employed for depositions. To eliminate the influence of wafer crystalline orientation on the film growth, c-Si substrates were covered with a 200 nm intrinsic poly-Si layer that was deposited by low-pressure chemical vapor deposition (LP-CVD) with high-temperature annealing at N<sub>2</sub> atmosphere. Native oxide on the poly-Si layer was removed by a short dip in 5 vol% HF solution before the depositions.

**Characterizations:** The XRD patterns were obtained by an automatic powder X-ray diffractometer X'Pert Pro equipped with an ultrafast linear semiconductor detector PIXcel and on a point proportional detector. Cu K $\alpha$  radiation ( $\lambda = 0.154$  nm) was used as an X-ray source. The X-ray incidence angle  $\omega$  was fixed at 0.5°. Raman spectra were recorded on a Renishaw InVia confocal Raman microscope with 633 nm laser excitation. Raman mapping was done in Streamline mode using a 50 $\times$  objective with a scan area of 20  $\times$  20  $\mu\text{m}^2$ . The acquisition time per scan was 10 s. The Raman spectra were fitted with Renishaw WiRE by using broadened Gaussian/Lorentzian line shapes, and corresponding Raman intensity maps were created from fitted results. Elemental compositions were analyzed by a Jeol JAMP 9510-F Auger microprobe at 10 keV energy with a tilt angle of 30° and 65° take-off angle. Depth profiling was conducted by sputtering with 1000 eV Ar<sup>+</sup> ions. SEI and BEI images were also recorded in topographic and compositional regimes using the same device. Root-mean-square roughness was measured by an atomic force microscope (AFM, NT-MDT nTegra). Nanostructural characterization of the cross-sectional samples was done using double corrected JEOL JEM ARM200cF STEM equipped with a cold field emission gun operated at 200 kV. All data were processed with Digital Micrograph GMS 3.21 (Gatan). EDS spectral images were acquired using a JEOL JED-2300 CENTURIO Silicon Drift Detector (SDD) collecting X-rays with an effective solid angle 0.98 sr and a detection area of 100 mm<sup>2</sup>. EDS measurements were performed using a probe current of 200 pA. The EDS energy range was 20 keV (10 eV/channel). EDS atomic maps with 256  $\times$  256 pixels were acquired with 200 frames and a 0.1 ms dwell time.

For electrical characterizations, Al contacts were deposited by vacuum thermal evaporation (PRO500S, Provac), and were subsequently annealed at 130 °C for 30 min to ensure ohmic contact. Resistivity and Hall effect measurements were conducted with van der Pauw geometry to determine the majority carrier type and concentration. A temperature-dependent current–voltage (*I*–*V*) setup was employed to measure the film conductivity. Wavelength-dependent reflectance and transmittance were obtained on a Perkin Elmer Lambda 950 UV-vis-NIR spectrometer single beam instrument over a range of 300–2500 nm. Absorbance was calculated by absorbance (%) = 100% – reflectance (%) – transmittance (%).

## Supporting Information

Supporting Information is available from the Wiley Online Library or from the author.

## Acknowledgements

The authors are indebted to Dr. G. Yang for substrate preparations and would like to thank M. Tijssen and S. G.M. Heirman for daily technical equipment supports. Y.T. acknowledges financial support from the China Scholarship Council (CSC).

## Conflict of Interest

The authors declare no conflict of interest.

## Keywords

BaSi<sub>2</sub>, heterostructures, photovoltaics, thin films

Received: May 19, 2020

Revised: July 6, 2020

Published online: August 6, 2020

- [1] T. Suemasu, *Jpn. J. Appl. Phys.* **2015**, *54*, 07JA01.
- [2] T. Suemasu, N. Usami, *J. Phys. D: Appl. Phys.* **2017**, *50*, 023001.
- [3] H. Schäfer, K. Janzon, A. Weiss, *Angew. Chem., Int. Ed.* **1963**, *2*, 393.
- [4] T. Goebel, Y. Prots, F. Haarmann, Z. Kristallogr. - New Cryst. Struct. **2009**, *224*, 7.
- [5] M. Kumar, N. Umezawa, W. Zhou, M. Imai, *J. Mater. Chem. A* **2017**, *5*, 25293.
- [6] K. Toh, T. Saito, T. Suemasu, *Jpn. J. Appl. Phys.* **2011**, *50*, 068001.
- [7] W. Du, R. Takabe, S. Yachi, K. Toko, T. Suemasu, *Thin Solid Films* **2017**, *629*, 17.
- [8] K. O. Hara, N. Usami, K. Nakamura, R. Takabe, M. Baba, K. Toko, T. Suemasu, *Appl. Phys. Express* **2013**, *6*, 112302.
- [9] R. Takabe, K. O. Hara, M. Baba, W. Du, N. Shimada, K. Toko, N. Usami, T. Suemasu, *J. Appl. Phys.* **2014**, *115*, 193510.
- [10] N. Shaalan, K. Hara, C. Trinh, Y. Nakagawa, N. Usami, *Mater. Sci. Semicond. Process.* **2018**, *76*, 37.
- [11] M. Kobayashi, K. Morita, T. Suemasu, *Thin Solid Films* **2007**, *515*, 8242.
- [12] M. Takeishi, Y. Matsumoto, R. Sasaki, T. Saito, T. Suemasu, *Phys. Proc.* **2011**, *11*, 27.
- [13] M. A. Khan, M. Takeishi, Y. Matsumoto, T. Saito, T. Suemasu, *Phys. Proc.* **2011**, *11*, 11.
- [14] K. O. Hara, N. Usami, Y. Hoshi, Y. Shiraki, M. Suzuno, K. Toko, T. Suemasu, *Jpn. J. Appl. Phys.* **2011**, *50*, 08LB03.
- [15] M. A. Khan, T. Saito, K. Nakamura, M. Baba, W. Du, K. Toh, K. Toko, T. Suemasu, *Thin Solid Films* **2012**, *522*, 95.
- [16] M. A. Khan, K. Hara, W. Du, M. Baba, K. Nakamura, M. Suzuno, K. Toko, N. Usami, T. Suemasu, *Appl. Phys. Lett.* **2013**, *102*, 112107.
- [17] K. O. Hara, N. Usami, M. Baba, K. Toko, T. Suemasu, *Thin Solid Films* **2014**, *567*, 105.
- [18] K. O. Hara, Y. Hoshi, N. Usami, Y. Shiraki, K. Nakamura, K. Toko, T. Suemasu, *Thin Solid Films* **2014**, *557*, 90.
- [19] Q. Deng, H. Chen, H. Liao, L. Chen, G. Wang, S. Wang, Y. Shen, *J. Phys. D: Appl. Phys.* **2019**, *52*, 075501.
- [20] K. Kodama, R. Takabe, T. Deng, K. Toko, T. Suemasu, *Jpn. J. Appl. Phys.* **2018**, *57*, 050310.
- [21] R. McKee, F. Walker, J. Conner, R. Raj, *Appl. Phys. Lett.* **1993**, *63*, 2818.
- [22] S. Yachi, R. Takabe, H. Takeuchi, K. Toko, T. Suemasu, *Appl. Phys. Lett.* **2016**, *109*, 072103.
- [23] R. Vismara, O. Isabella, M. Zeman, *Opt. Express* **2017**, *25*, A402.
- [24] J.-S. Huang, K.-W. Lee, Y.-H. Tseng, *J. Nanomater.* **2014**, *2014*, 238291.
- [25] M. A. Green, E. D. Dunlop, J. Hohl-Ebinger, M. Yoshita, N. Kopidakis, A. W. Y. Ho-Baillie, *Prog. Photovoltaics Res. Appl.* **2020**, *28*, 3.
- [26] N. A. A. Latiff, T. Yoneyama, T. Shibutani, K. Matsumaru, K. Toko, T. Suemasu, *Phys. Status Solidi C* **2013**, *10*, 1759.
- [27] T. Yoneyama, A. Okada, M. Suzuno, T. Shibutani, K. Matsumaru, N. Saito, N. Yoshizawa, K. Toko, T. Suemasu, *Thin Solid Films* **2013**, *534*, 116.
- [28] K. O. Hara, Y. Nakagawa, T. Suemasu, N. Usami, *Jpn. J. Appl. Phys.* **2015**, *54*, 07JE02.
- [29] Y. Tian, R. Vismara, S. Van Doorene, P. Šutta, L. Vančo, M. Veselý, P. Vogrinčič, O. Isabella, M. Zeman, *ACS Appl. Energy Mater.* **2018**, *1*, 3267.



- [30] T. Yoshitake, T. Nagamoto, K. Nagayama, *Thin Solid Films* **2001**, 381, 236.
- [31] Y. Tian, A. R. Montes, L. Vančo, O. Isabella, M. Zeman, *Jpn. J. Appl. Phys.* **2020**, 59, SFFA03.
- [32] A. G. Birdwell, R. Glosser, D. N. Leong, K. P. Homewood, *J. Appl. Phys.* **2001**, 89, 965.
- [33] G. Faraci, S. Gibilisco, P. Russo, A. R. Pennisi, S. La Rosa, *Phys. Rev. B* **2006**, 73, 033307.
- [34] T. Sato, H. Hoshida, R. Takabe, K. Toko, Y. Terai, T. Suemasu, *J. Appl. Phys.* **2018**, 124, 025301.
- [35] C. Hayzelden, J. Batstone, R. Cammarata, *Appl. Phys. Lett.* **1992**, 60, 225.
- [36] C. Hayzelden, J. Batstone, *J. Appl. Phys.* **1993**, 73, 8279.
- [37] R. Takabe, T. Deng, K. Kodama, Y. Yamashita, T. Sato, K. Toko, T. Suemasu, *J. Appl. Phys.* **2018**, 123, 045703.
- [38] A. Yelon, B. Movaghar, *Phys. Rev. Lett.* **1990**, 65, 618.